Theoretical and electrochemical studies on organometallic symmetrical Schiff base complexes of Zn(II), Cu(II), Ni(II) and Co(II)†

Mauricio Fuentealba,*[a,b] María Teresa Garland,[b,c] David Carrillo,[a] Carolina Manzur,*[a] Jean-René Hamon[d] and Jean-Yves Saillard*[d]

Received 26th July 2007, Accepted 27th September 2007
First published as an Advance Article on the web 17th October 2007
DOI: 10.1039/b711467b

The electronic communication between two redox centres through a Schiff base complex has been investigated in a series of ethylenediimine-bis(1-ferrocenyl-1,3-butanedionate) complexes of Zn(II) **1**, Cu(II) **2**, Ni(II) **3** and Co(II) **4**. Cyclic voltammetry experiments of **1** and **2** exhibit a unique two-electron reversible oxidation wave, whereas in the case of **3** and **4** two and three one-electron oxidation processes are, respectively, observed. These results suggest some electronic interaction between the iron atoms of the ferrocenyl groups. DFT calculations carried out on model complexes show that for all the studied compounds the removal of the first two electrons corresponds to the oxidation processes of the iron centres in the weakly coupled ferrocenyl termini. The electronic communication between the two iron centres increases on going from **1** to **4**. Finally, a re-indexation of the bands observed in the UV-Visible spectra has been carried out using TDDFT calculations.

Introduction

In the field of electronic communication between metal atoms several examples where two ferrocenyl moieties are linked through organic[1] or inorganic[2] spacers have been reported and experimental and theoretical studies have focused on the nature of the bridge in the electronic interactions between the redox centres. Ten years ago, Zanello *et al.* investigated the electronic communication between two ferrocenyl fragments through bis(β-diketonate) transition metal complexes.[3] These complexes exhibit a single reversible two-electron oxidation wave indicating the absence of electronic communication between both ferrocenyl units. On the other hand, the complex bis(1-ferrocenyldithiolene)nickel(II) undergoes two monoelectronic oxidation processes attributed to the ferrocenyl groups.[4] This observation shows that the bis(dithiolene)nickel(II) core serves as an efficient bridge for electronic communication between the ferrocenyl redox centres. In both cases, the shortest pathway between the two ferrocenyl moieties is six covalent bonds suggesting that predominant factors in the electronic communication between two redox centres are the coordination sphere geometries and/or the nature of the metal centre, the distance between the metals being less important. In this context, and in order to get a deeper insight into the interaction between two redox centres through a Schiff base complex, we have revisited the chemistry of the symmetrical ethylenediimine-bis(1-ferrocenyl-1,3-butanedionate) complexes of Zn(II) **1**, Cu(II) **2**, Ni(II) **3** and Co(II) **4** that has been previously reported.[5] The rigidity of the ethylenediimine fragment is expected to induce a better electronic communication between the two terminal redox centres. These complexes were fully characterized by spectroscopic techniques and, for complexes **2** and **3**, authenticated by single crystal X-ray diffraction analysis. To the best of our knowledge, the redox properties of these potentially mixed valence systems have not been explored elsewhere. In this work we report the redox properties and DFT investigation of this series of complexes.

Results and discussion

Synthesis

In order to simplify the experimental procedure, the syntheses of complexes **1–4** were performed in an one-step templated reaction mixing the compounds 1-ferrocenyl-1,3-butanedione, ethylenediamine and the metal(II) acetate, in a molar ratio of 2 : 2 : 1, in refluxing methanol for 15 h (Scheme 1). This procedure afforded the compounds in good yields (44–58%).

The complexes are soluble in chloroform, methylene chloride, acetone and insoluble in non-polar solvents such as hexane, diethyl ether and toluene. Considering that complexes **1–4** were previously reported,[5] a discussion of the spectroscopic characterization is not pertinent here.

Electronic spectroscopy

Electronic spectra of complexes **1–4** have been previously reported by Ying *et al.*[5a] and, by Shi *et al.*[5b] for complexes **2** and **3**. In both papers the electronic spectra have been recorded in dimethylformamide (DMF) solutions and the assignments of the electronic transitions are contradictory. Ying *et al.* assigned the highest energy bands to the cyclopentadienyl ring B-band

[a]*Laboratorio de Química Inorgánica, Instituto de Química, Pontificia Universidad Católica de Valparaíso, Avenida Brasil 2950, Valparaíso, Chile. E-mail: cmanzur@ucv.cl*
[b]*Laboratorio de Cristalografía, Departamento de Física, Facultad de Ciencias Físicas y Matemáticas, Universidad de Chile, Avenida Blanco Encalada 2008, Santiago, Chile*
[c]*Centro para la Investigación Interdisciplinaria Avanzada en Ciencias de los Materiales (CIMAT), Universidad de Chile, Avenida Blanco Encalada 2008, Santiago, Chile*
[d]*Université de Rennes 1, CNRS UMR 6226 Sciences Chimiques de Rennes, Campus de Beaulieu, 35042 Rennes-cedex, France. E-mail:saillard@univ-rennes1.fr*
† CCDC reference number 655308. For crystallographic data in CIF or other electronic format see DOI: 10.1039/b711467b

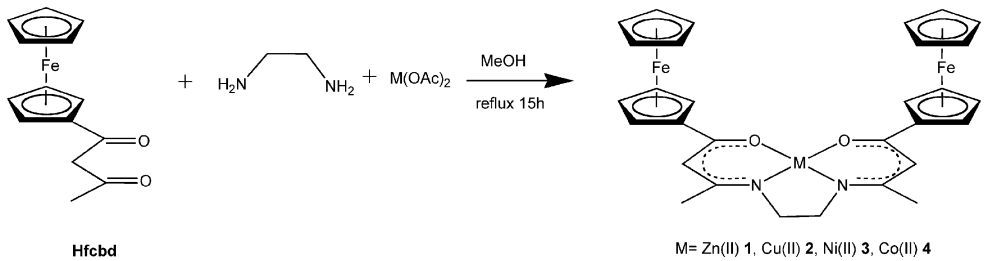

Scheme 1 Preparation of complexes **1–4**.

and to the K-band of the ligand. A lower energy band was assigned to charge transfer in the ferrocenyl group and the lowest energy band was attributed to a d–d transition of the metal ions. On the other hand, Shi *et al.* assigned also the highest energy bands to the B-band and the K-band, but attributed the lowest energy transition of **2** (446 nm) to a ligand-to-metal charge transfer (LMCT) transition. However, for **3** no LMCT transition was assigned by these authors. To elucidate this controversy, we recorded the electronic spectra of **1–4** in CH_2Cl_2 solutions to avoid the coordination effect of solvent such as DMF. Their absorption maxima and log ε are summarized in Table 1.

We observed two sets of deconvoluted bands for all the complexes: (i) a set of 2–3 bands between 231 and 380 nm attributed to the intra-ligand charge transfer transitions, LMCT transitions from the ligand to the ferrocenyl groups or MLCT from the metal centre to the ligand and d–d transitions, (ii) a low-energy band attributed to metal-to-ligand charge transfer transitions from the ferrocenyl groups to the ligand. These assignments are supported by TDDFT calculations (*vide infra*).

Electrochemical studies

The redox properties of complexes **1–4** were explored by cyclic voltammetry (see Experimental for details). The half-wave potentials of the redox processes are summarized in Table 2. Co(II), **4**, and Ni(II), **3**, complexes undergo three and two one-electron oxidation processes, respectively, whereas Cu(II), **2**, and Zn(II), **1**, complexes exhibit a unique two-electron oxidation process (see Fig. 1). The one- and two-electron nature of the oxidation processes were confirmed by determining the ratio between the integrated area of the oxidation waves with that of ferrocene under the same electrochemical conditions, assuming rather close diffusion coefficients for ferrocene and the four neutral species under investigation. Those are 2.18, 2.08, 1.85 and 2.85 for **1**, **2**, **3** and **4**, respectively. All these redox processes are chemically reversible, as evidenced by the following criteria: (i) the current ratios i_{pa}/i_{pc} are constantly equal to 1, (ii) the current functions $i_{pa}/V^{1/2}$ remain constant, and (iii) for **3** and **4**, the peak-to-peak separations ΔE_p are very close to the 81 mV value determined for the internal ferrocene standard (see Table 2). Bulk anodic electrolyses carried out at 293 K with E_{appl} = 1.1 V gave 2.0 F equiv.$^{-1}$ for **3** whereas only 1.0 F equiv.$^{-1}$ was found for **4**. This latter observation could be explained by a fast follow-up reaction of the electrogenerated cation $\mathbf{4}^+$. In both cases, formation of a precipitate was noted upon completion of the electrolyses. The lack of stability of the different cations on the long time scale of controlled potential coulometric measurements was clearly

Table 1 Electronic spectra data of **1–4**

Complex	λ_{max}/nm (log ε)	Complex	λ_{max}/nm (log ε)
1	271 (3.91) 322 (4.14) 350 (4.19) 458 (3.24)	**3**	292 (4.16) 334 (4.10) 398 (3.78) 450 (3.41) 480 (3.22)
2	282 (3.88) 334 (4.28) 370 (4.14) 450 (3.44)	**4**	267 (4.12) 337 (4.34) 358 (3.57) 410 (3.24) 461 (3.53)

Table 2 Electrochemical data[a] for compounds **1–4**

Compound	$E_{1/2}$/mV (ΔE/mV)[b]
1	532(144)[c]
2	491(194)[c]
3	483(68)
	566(71)
4	348(92)
	535(98)
	636(72)

[a] Recorded in dichloromethane at 293 K with a Pt working electrode, with 0.1 M n-$Bu_4N^+PF_6^-$ as supporting electrolyte; all potentials are *vs.* Ag/AgCl, scan rate = 0.1 V s^{-1}. [b] Peak-to-peak separation between the resolved reduction and oxidation wave maxima. [c] Two-electron wave.

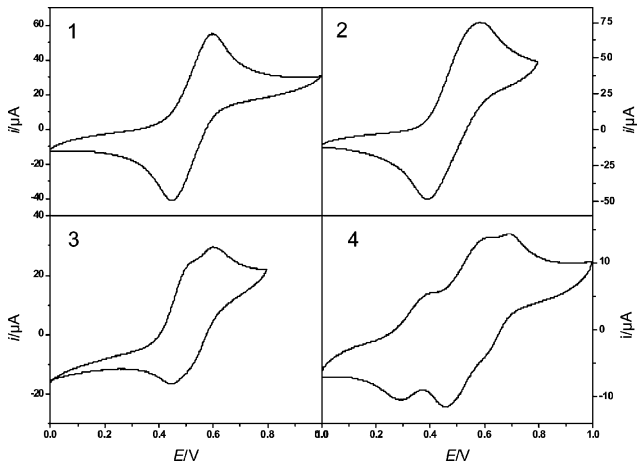

Fig. 1 Cyclic voltammograms of complexes **1–4** recorded in CH_2Cl_2–0.1 M n-$Bu_4N^+PF_6^-$ at T = 293 K and a voltage sweep rate v = 0.1 V s^{-1}, reference electrode Ag/AgCl.

demonstrated by cyclic voltammetric controls which did not show the reduction processes of the starting materials.

Unexpectedly, the first oxidation process of complex **4** is shifted to a more cathodic potential compared to the potential value of the first oxidation process of complexes **1–3**. This behaviour can be explained considering the mixing of Fe(II) and Co(II) levels of the first doubly occupied molecular orbital of complex **4** (see Theoretical section below).

The first process in complexes **1–4** is attributed to the oxidation of one ferrocenyl moiety (*vide infra*). In complexes **1** and **2** these oxidation waves correspond to two-electron processes indicating the simultaneous removal of two electrons, one for each ferrocenyl group. No oxidation to more anodic potentials was observed up to the higher limit of the potential interval considered in the experimental measurements. In complex **3**, the second oxidation process, shifted 83 mV to a more anodic potential, is attributed to the removal of one electron on the second ferrocenyl group. Finally, in the Co(II) complex, **4**, the second oxidation process, shifted 187 mV to a more anodic potential, is also attributed to the second ferrocenyl group, while the third process is attributed to the one-electron oxidation of Co(II).

In the case of two ferrocenyl moieties, with identical chemical ambiance and connected by a symmetrical spacer, the potential values of the oxidation processes are indicative of the extension of electronic cooperativity between the organometallic fragments.[6] For complexes **1** and **2** the occurrence of a sole reversible oxidation process for two electrons indicates the lack of interaction between the ferrocenyl moieties. In the case of complexes **3** and **4** the appearance of two and three oxidation waves, respectively, shows some degree of electronic cooperativity. The comparison between the comproportionation constant (K_c) values in symmetric dinuclear complexes has been used as a measure of stability of the mixed-valence species generated upon one-electron oxidation of a dinuclear complex. The K_c can be calculated exclusively with the data obtained from cyclic voltammetry studies using the equation $\Delta G = -RT(\ln K_c) = -nF(\Delta E_{ox})$ and the calculated values for compounds **3** and **4** are 25 and 1450, respectively. These data indicate that the mixed-valence species $\mathbf{4}^+$ is more stable than $\mathbf{3}^+$. Nevertheless, the data obtained exclusively from cyclic voltammetry may not be applied with accuracy in all the symmetric systems.[7] All the attempts to isolate mixed-valence compounds generated using redox chemical oxidizing agents failed. Upon addition of 0.5 equiv. $AgPF_6$ to a methylene chloride solution of **3** or **4**, the characteristic dark blue–violet color of the ferricinium salts developed immediately along with simultaneous precipitation of metallic silver, clearly indicating the oxidation of the orange–red starting materials. The IR spectra of the isolated products displayed the strong and medium intensity bands at 840 and 558 cm^{-1} unambiguously assigned to ν(P–F) and $\delta(PF_6)$ stretching and bending modes of the PF_6^- counteranion, respectively, while the ^1H NMR spectra showed several ill-resolved signals attributable to a mixture of diamagnetic and paramagnetic compounds. Thus, side reactions occur upon electron transfer confirming the results of the controlled potential coulometric measurements.

Crystallography

Single crystals of **3** suitable for X-ray diffraction were obtained by slow diffusion of diethyl ether into a concentrated dichloromethane solution of the complex. Fig. 2 shows an ORTEP drawing of molecule **3** with atomic numbering scheme. Selected bond lengths and bond angles are listed in Table 3. The molecule crystallizes in the monoclinic space group $C2/c$ with only one molecule per asymmetric unit. Interestingly, compound **3** appears as a polymorphic variation of that reported by Shi *et al.*[5b] However, the metrical values of the two symmetrical Schiff base complexes are identical within the error of the measurement. Complex **3** can be described as a classical *cis*-N_2O_2 symmetrical Schiff base derived from the 2 : 1 condensation between a β-diketone and ethylenediamine, with two pendant ferrocenyl moieties.

Table 3 Selected bond distances (Å) and bond angles (°)

Ni(1)–N(1)	1.835(8)	C(16)–C(15)–N(1)	111.4(9)
Ni(1)–N(2)	1.857(8)	C(15)–C(16)–N(2)	109.9(9)
Ni(1)–O(1)	1.848(6)	N(1)–Ni(1)–O(1)	95.5(3)
Ni(1)–O(2)	1.850(6)	N(1)–Ni(1)–N(2)	87.2(4)
C(20)–O(1)	1.264(10)	O(1)–Ni(1)–O(2)	82.6(3)
C(11)–O(2)	1.298(11)	O(1)–Ni(1)–N(2)	177.1(3)
C(13)–N(1)	1.338(12)	O(2)–Ni(1)–N(1)	177.8(3)
C(17)–N(2)	1.302(12)	N(2)–Ni(1)–O(2)	94.7(3)
C(15)–N(1)	1.493(11)	Cp_{CNT}–Fe(1)–C_5H_{4CNT}	178.1
C(16)–N(2)	1.488(12)	Cp_{CNT}–Fe(2)–C_5H_{4CNT}	177.2

Abbreviations: Cp = C_5H_5, CNT = centroid.

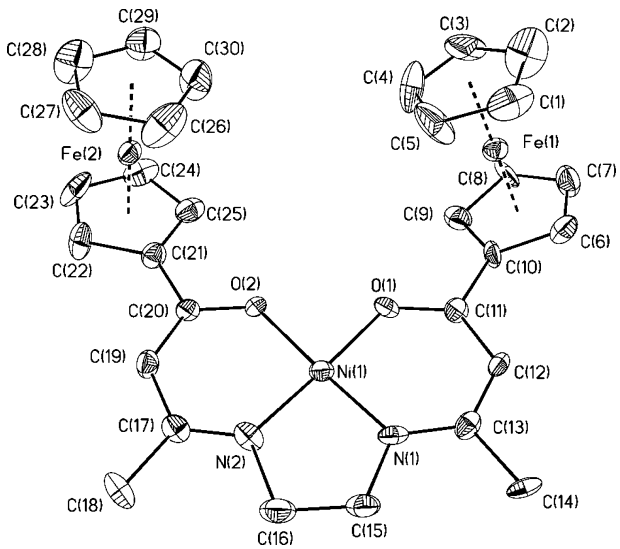

Fig. 2 ORTEP plot and atom numbering scheme of **3**. The thermal ellipsoids have a 30% probability. Hydrogen atoms have been omitted for clarity.

This kind of compound has four possible isomers: (i) two with the ferrocenyl fragments in *syn* or *anti* positions, and (ii) two additional isomers with the coordination sphere around the nickel(II) atom adopting a square-planar or a pseudo-tetrahedral geometry. Unlike the analogous copper complex[5] in which the *syn* and *anti* isomers are observed in the same asymmetric unit, in our case, we observe only the *syn* conformation in the crystalline system probably because of stacking between two molecules which form dimeric units (*vide infra*). It should be noted that the difference in energy between the *syn* and *anti* conformations is found to be less than 1 kcal mol^{-1} by DFT calculations (see below).

On the other hand, the nickel atom exhibits a square-planar geometry, as shown by: (i) the almost identical bond lengths associated to the nickel atom (see Table 3) (ii) the displacement of the nickel atom by only 0.003 Å away from the N_2O_2 least-squares plane and (iii) the sum of the four angles around the nickel atom which is 360°. Moreover, the largest displacement from the NiO_2N_2 least-squares plane is 0.018 Å and associated with O(2).

In the crystal, molecules of compound **3** are packed to form centrosymmetric pairs (symmetry operator: $-x$, $-y$, $-z$; see Fig. 3), with a separation between the NiN_2O_2 least-squares planes equal to 3.470 Å. The shortest intermolecular distance between two atoms of the symmetry related molecules is 3.478(7) Å between Ni(1) and N(2A), and the Ni(1)···Ni(1A) separation is 3.761(2) Å, excluding any significant interaction between the metal ions. Such a difference of 0.283 Å between these two values is accounted for by the component molecules only very slightly displaced parallel to their long axis. This situation is similar to that which we reported previously for a binuclear unsymmetrical Schiff base complex containing the same ferrocenyl enaminoketonate subunit.[8]

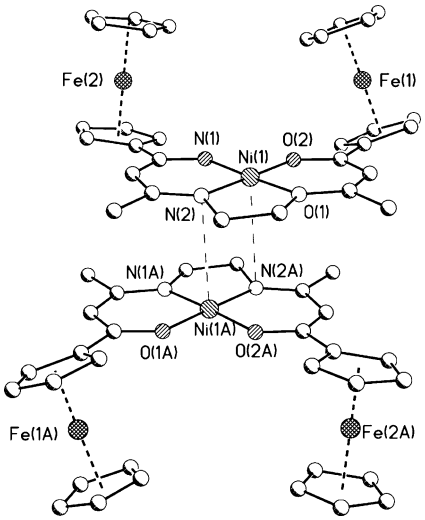

Fig. 3 Ball-and-stick plot of two molecules of **3** forming a dimeric unit. Hydrogens atoms have been omitted for clarity. Symmetry transformations used to generate equivalent atoms A: $-x$, $-y$, $-z$.

Finally, the ferrocenyl groups exhibit an eclipsed conformation of the cyclopentadienyl ligands. The ring centroid to iron distances for the substituted and unsubstituted cyclopentadienyl rings are 1.638 and 1.627 Å for Fe(1) and 1.648 and 1.627 Å for Fe(2), respectively. In both ferrocenyl subunits the C_5-rings are essentially coplanar with C_5-ring centroid–Fe–C_5-ring centroid angles of 178.1° and 177.2° for Fe(1) and Fe(2), respectively. These metrical values are typical for a η^5-Fe-η^5 coordination.[9]

Theoretical investigations

In order to provide a better understanding of the redox properties of these symmetrical bis(ferrocenyl)diimine-complexes of Zn(II) **1**, Cu(II) **2**, Ni(II) **3** and Co(II) **4**, we have carried out DFT calculations on a series of simplified models for complexes **1–4** in which the methyl groups have been replaced by hydrogen atoms (see Scheme 2). These model complexes are labelled **1′**, **2′**, **3′** and **4′**, respectively. Calculations have been performed on the neutral and on the mono- and di-oxidized forms of these models. Selected computed data are given in Tables 4–7.

Table 4 Major computed data for $\mathbf{1'}^{0/+/2+}$

	$\mathbf{1'}$	$\mathbf{1'}^{+}$	$\mathbf{1'}^{2+}$
HOMO-LUMO gap/eV	1.90	—	—
Ionization potentials/eV	—	7.09	9.20
	Bond distances (Å) and angles (°)		
Zn–O	1.998, 2.002	2.007, 2.003	2.013, 2.011
Zn–N	2.053, 2.053	2.055, 2.059	2.059, 2.065
Cp_{CNT}–Fe	1.695, 1.694	1.732, 1.729	1.752, 1.751
Fe–C_5H_{4CNT}	1.685, 1.687	1.724, 1.722	1.746, 1.744
Dihedral angle/°			
O–Zn–N/O′–Zn–N′	19	21	22
	Mulliken charges [spin density]		
Cp and C_5H_4 rings	0.03	−0.06 [−0.18]	0.66 [−0.34]
Fe1	0.03	0.52 [0.57]	0.51 [1.02]
Fe2	0.06	0.52 [0.55]	0.52 [1.01]
Ligand	−0.86	−0.82 [0.07]	−0.54 [0.31]
Zn	0.75	0.84 [−0.01]	0.86 [0.00]

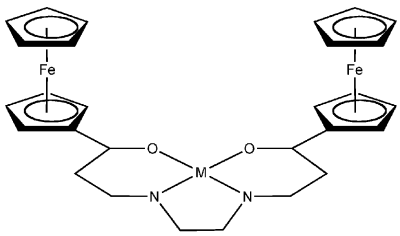

M= Zn **1'**, Cu **2'**, Ni **3'**, Co **4'**

Scheme 2 Model complexes used in the calculations.

Among the **1–4** series, the X-ray crystal structures of the nickel complex **3** and of the copper complex **2** are known (*vide supra*). **3** exhibits a *syn* conformation in the solid state, whereas in the case of **2** both *syn* and *anti* rotamers have been shown to exist in the same crystal.[5] We have optimized the geometries of the model **3′** in the *syn* and *anti* conformations. Both conformations were found to be almost isoenergetic, their energy difference being lower than 1 kcal mol^{-1}, a value which is not significant at the considered level of theory. Moreover, a careful analysis of their electronic structures indicated almost identical characteristics. Therefore, it was chosen to carry out the calculations on the whole **1′–4′** series in the *syn* conformation. The calculations were made without any symmetry constrain. This allowed more flexibility to the metal coordination sphere and to the bridging Schiff base complex. Nevertheless, a rough C_s pseudo-symmetry can be considered for the whole series, as exemplified by the optimized structures of **1′** and **4′** which are shown in Fig. 4.

The optimized bond distances obtained for **2′** and **3′** are in good agreement with the experimental X-ray values of **2**[5b] and **3**, respectively. A remarkable difference between the optimized geometries of **1′** and **2′–4′** is the dihedral angle formed by the O–M–N and O′–M–N′ planes. In the case of **2′–4′** the metal coordination sphere is almost planar (dihedral angle ≤6°) while in the case of **1′** the angle is significantly larger (16°). This difference is related to the preference of the four-coordinate d^{10} Zn(II) to be

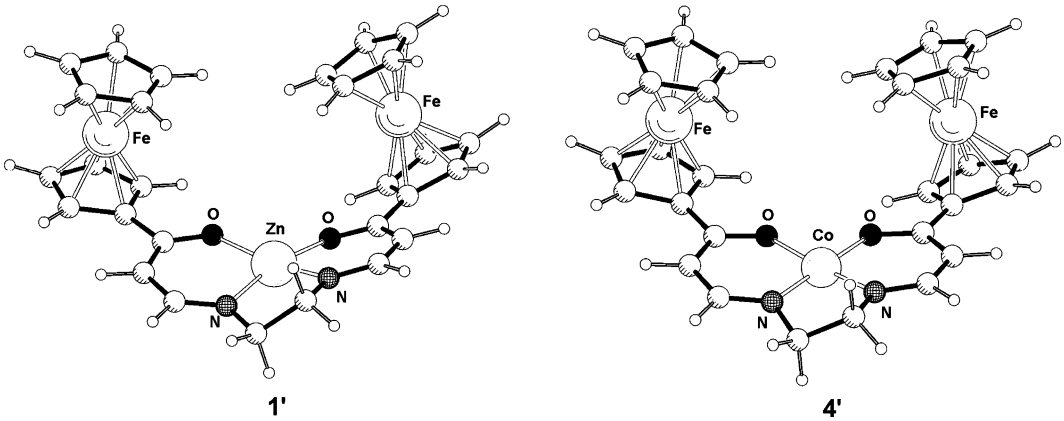

Fig. 4 Optimized geometries of **1**′ and **4**′.

tetrahedral. However, one is very far from the value of 90° that would be required for ideal tetrahedral coordination. This result nicely illustrates the rigidity effect induced by the ethylene bridge on the chelating ligand. Whatever the metal electron count, the planar or approximately planar coordination is maintained by the ligand.

The MO diagrams of the **1**′–**4**′ series are shown in Fig. 5. For simplicity, the diagrams of the odd-electron species **2**′ and **4**′ correspond to spin-restricted calculations, whereas all their other computed data given in this paper correspond to spin-unrestricted calculations (see Computational details). For the sake of comparison the energies of the HOMOs have all been arbitrarily set to zero. The HOMO–LUMO gap of the zinc(II) complex **1**′ is large (1.90 eV). The six highest occupied orbitals are largely localized on the iron atoms and correspond to the so-called non-bonding "t_{2g}" combinations of the two ferrocenyl moieties. The five d-type zinc levels lie at a much lower energy. The two lowest vacant levels are the combinations of the π*(CN) and π*(CO) orbitals of the ligand which can be considered as antisymmetric with respect to the molecular pseudo-mirror. The so-called Fe "e_g*" combinations (antibonding d-type MOs) constitute the LUMO+2 to LUMO+5 group (Fig. 5). Thus, the oxidation of **1**′ by one and two electrons corresponds essentially to the oxidation of the iron centres. The SOMO of $\mathbf{1}'^{+}$ (unrestricted spin orbital) is shown in Fig. 6. It can be described as an in-phase combination of Fe $d_{x^2-y^2}$ orbitals, with similar localization on both centres (40% and 36%). Consistently, the computed Fe spin densities are also comparable (0.57 and 0.55, see Table 4). Despite all our broken symmetry trials, it was not possible to localize the single electron on a particular iron centre. Thus, at the considered level of theory, $\mathbf{1}'^{+}$ is a delocalized mixed-valent compound. The ground state of $\mathbf{1}'^{2+}$ was found to be a delocalized triplet state, with the two singly occupied MOs being the in-phase and out-of-phase combinations of the Fe $d_{x^2-y^2}$ orbitals. The corresponding occupied spin orbitals are shown in Fig. 6. Consistently with the iron atoms being the oxidized centres, the spin density of the oxidized species is localized exclusively on the iron atoms (Table 4). The computed bond distances are also consistent with this trend since the calculated Zn–O and Zn–N distances remains virtually unchanged upon oxidation, while at the same time the Fe cyclopentadienyl distances are somewhat lengthened (Table 4).

Although the Cu(II) complex **2**′ has the same number of electrons as $\mathbf{1}'^{+}$, it has a somewhat different electronic structure. Indeed, the SOMO is copper (not iron) centred. It can be described as an antibonding combination of the Cu $d_{x^2-y^2}$ orbital with the proper combination of the ligand lone pairs. It has a participation of 48% on Cu (see Fig. 6), consistent with the Cu and ligand spin density values, 0.46 and 0.51, respectively (see Table 5).

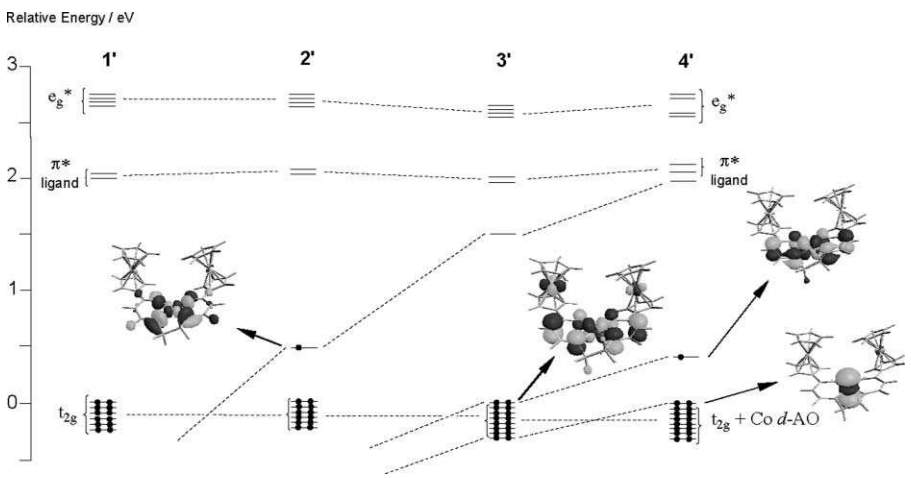

Fig. 5 Computed MO diagrams of the **1**′–**4**′ models. The HOMO energies have been arbitrarily set to zero for clarity.

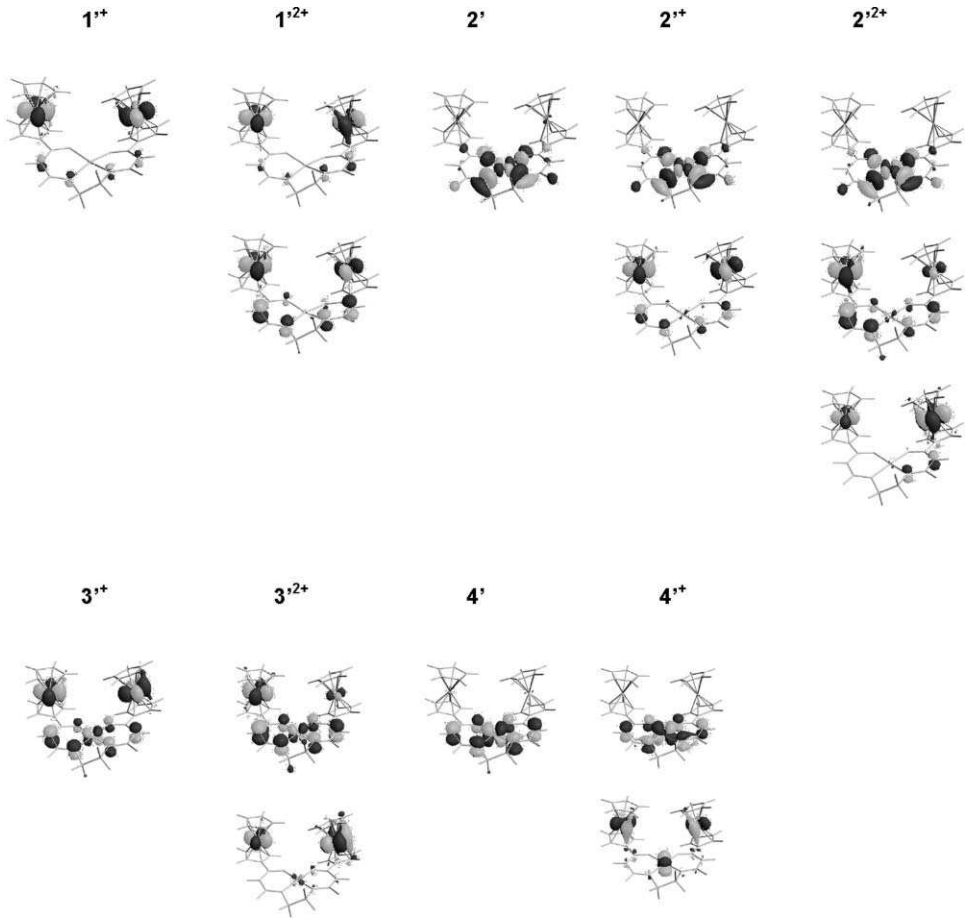

Fig. 6 Plots of the singly occupied orbitals of $\mathbf{1}'^{+/2+}$, $\mathbf{2}'^{0/+/2+}$, $\mathbf{3}'^{+/2+}$ and $\mathbf{4}'^{0/+}$ (spin-unrestricted calculations).

This is a typical situation for a d^9 Cu(II) square-planar complex. All the others MOs remain unchanged when compared to $\mathbf{1}'^{+}$. Interestingly, the oxidation of $\mathbf{2}'$ by one and two electrons leaves the SOMO occupation unchanged and corresponds essentially to the oxidation of the iron centres, $\mathbf{2}'^{+}$ and $\mathbf{2}'^{2+}$, which were found to be a triplet and a quadruplet state, respectively. At the considered level of theory, both model complexes have similar delocalized mixed-valent iron centres (Table 5), as in the $\mathbf{1}'^{+/2+}$ series. They only differ from their Zn(II) homologues by the occupation of the level derived from the central metal $d_{x^2-y^2}$ AO which is singly occupied in the case of Cu and fully occupied (and low-lying) in the case of Zn. The computed spin densities of the $\mathbf{2}'^{0/+/2+}$ series are consistent with the Fe(II)Cu(II)Fe(II), Fe(2.5)Cu(II)Fe(2.5) and Fe(III)Cu(II)Fe(III) oxidation states, respectively.

The LUMO of the Ni(II) model complex $\mathbf{3}'$ corresponds to the SOMO of $\mathbf{2}'$, but lies at higher energy with respect to the next occupied level. Hence, $\mathbf{3}'$ is a singlet state secured by a large HOMO–LUMO gap (Fig. 5). The HOMO of $\mathbf{3}'$ is nickel(II) centred. It is made of a d_π orbital (43%) mixed in an antibonding way with π-type ligand orbitals (35%). It has also a small Fe participation (11%). The six Fe "t_{2g}" combinations lie just below the HOMO. The three other Ni(II) levels are at lower energies. Despite of the Ni(II) nature of its HOMO, the one- and two-electron oxidations of $\mathbf{3}'$ correspond to the depopulations of Fe "t_{2g}" orbitals. As in the case of $\mathbf{1}'^{2+}$, $\mathbf{3}'^{2+}$ was found to be a triplet state. The singly occupied orbitals of $\mathbf{3}'^{+}$ and $\mathbf{3}'^{2+}$ are shown in Fig. 6. The calculated spin densities of $\mathbf{3}'^{+}$ and $\mathbf{3}'^{2+}$ (Table 6) are consistent with the Fe(2.5)Ni(II)Fe(2.5) and Fe(III)Ni(II)Fe(III) oxidation states. However, some contribution of the Ni(II) centre to the spin density can be traced. This is due to the closer proximity in energy of the 3d(Ni) and 3d(Fe) orbitals which favours mixing between these orbitals. A similar effect is expected to be larger in the case of the Co(II) complex.

Table 5 Major computed data for $\mathbf{2}'^{0/+/2+}$

	$\mathbf{2}'$	$\mathbf{2}'^{+}$	$\mathbf{2}'^{2+}$
Ionization potentials/eV	—	7.03	9.25
	Bond distances (Å) and angles (°)		
Cu–O	1.981, 1.977	1.989, 1.982	1.987, 1.985
Cu–N	1.966, 1.974	1.971, 1.977	1.972, 1.975
Cp_{CNT}–Fe	1.697, 1.694	1.725, 1.724	1.755, 1.756
Fe–C_5H_{4CNT}	1.686, 1.685	1.718, 1.717	1.748, 1.743
Dihedral angle/°			
O–Cu–N/O′–Cu–N′	4	7	7
	Mulliken charges [spin density]		
Cp and C_5H_4 rings	0.03 [0.03]	−0.07 [−0.15]	0.65 [−0,31]
Fe1	0.02 [0,00]	0.51 [0.52]	0.50 [0.98]
Fe2	0.05 [0,00]	0.52 [0.52]	0.52 [0.99]
Ligand	−0.80 [0.51]	−0.72 [0.65]	−0.45 [0.87]
Cu	0.70 [0.46]	0.76 [0.46]	0.78 [0.46]

Table 6 Major computed data for $\mathbf{3'}^{0/+/2+}$

	$\mathbf{3'}$	$\mathbf{3'}^{+}$	$\mathbf{3'}^{2+}$
HOMO–LUMO gap/eV	1.43	—	—
Ionization potentials/eV	—	6.99	9.12
	Bond distances (Å) and angles (°)		
Ni–O	1.900, 1.900	1.901, 1.901	1.905, 1.903
Ni–N	1.870, 1.871	1.866, 1.869	1.869, 1.869
Cp_{CNT}–Fe	1.695, 1.692	1.720, 1.715	1.748, 1.747
Fe–C_5H_{4CNT}	1.686, 1.684	1.713, 1.715	1.746, 1.746
Dihedral angle/°			
O–Ni–N/O′–Ni–N′	6	6	5
	Mulliken charges [spin density]		
Cp and C_5H_4 rings	0.03	−0.14 [−0.14]	0.58 [−0.28]
Fe1	0.02	0.51 [0.42]	0.49 [0.86]
Fe2	0.05	0.53 [0.43]	0.52 [0.90]
Ligand	−0.67	−0.59 [0.17]	−0.31 [0.32]
Ni	0.57	0.70 [0.12]	0.74 [0.20]

Table 7 Major computed data for $\mathbf{4'}^{0/+}$

	$\mathbf{4'}$	$\mathbf{4'}^{+}$
Ionization potentials/eV		5.70
	Bond distances (Å) and angles (°)	
Co–O	1.893, 1.889	1.898, 1.885
Co–N	1.858, 1.856	1.856, 1.856
Cp_{CNT}–Fe	1.697, 1.693	1.721, 1.717
Fe–C_5H_{4CNT}	1.687, 1.686	1.710, 1.708
Dihedral angle/°		
O–Co–N/O′–Co–N′	4	4
	Mulliken charges [spin density]	
Cp and C_5H_4 rings	0.01 [0.00]	0.72 [−0.16]
Fe1	0.02 [−0.01]	−0.01 [0.43]
Fe2	0.05 [−0.01]	0.02 [0.42]
Ligand	−0.76 [0.12]	−0.48 [0.19]
Co	0.68 [0.90]	0.75 [1.12]

The SOMO of the Co(II) model complex $\mathbf{4'}$ is similar to the HOMO of $\mathbf{3'}$. It has a 62% participation on Co(II), in agreement with a large Co(II) spin density (Table 7). However, the next occupied level is also Co(II) centred (Fig. 4). It is essentially a non bonding d_{z^2} orbital (84%). The following occupied levels can be identified as the "t_{2g}" combinations with some Co(II) contamination. The removal of one electron from $\mathbf{4'}$ yields a triplet state. The highest SOMO of $\mathbf{4'}^{+}$ is similar to the SOMO of $\mathbf{4'}$. It is predominantly Co localized (69%) with no Fe participation. On the other hand, the second SOMO has a mixed Fe (28% and 29%) and Co (24%) character, with very little bridge participation. Thus, the one-electron oxidation affects the three metal centres, primarily the iron ones, but also the Co centre, as also exemplified by the spin densities reported in Table 7. Unfortunately, we were unable to make the calculations on $\mathbf{4'}^{2+}$ to converge. This problem is likely to be related to numerical instability in the self-consistent process due to the superposition in energy of the 3d Co and Fe levels.

Thus, except for the Co(II) model species $\mathbf{4'}$, the first two one-electron oxidation processes involve essentially the iron centres. Consistently, the computed first and second ionization potentials are quite similar for the three compounds (Tables 4–7). The second potentials are significantly larger than the first ones. This is at least in part related to the delocalized nature of the mixed-valent state. However, this delocalization is not important in the case of the Zn(II) and Cu(II) species, as exemplified by the corresponding SOMO plots of $\mathbf{1'}^{2+}$ and $\mathbf{2'}^{2+}$ in Fig. 6. Through-space (~7.5 Å) and/or through-bridge electrostatic interactions between the iron centres are also likely to play some role in the preference for delocalized Fe(III)···Fe(III) systems in the dicationic species. However, the computed results appear to be inconsistent with the cyclovoltammetric data which show only one single 2-electron oxidation wave for **1** and **2** (*vide supra*). Such an apparent inconsistency between computed ionization potentials and observed redox potentials is not uncommon in transition-metal chemistry.[10] It is usually related to the fact that the computed data do not take into account solvent and electrolyte effects. In this particular case, we believe that electrolyte effects play a crucial role in the wave separations, as it has been demonstrated on related organometallic systems.[11] The fact that **3** exhibits two separate one-electron oxidation waves can be related to the participation of the central metal to the spin delocalization found in $\mathbf{3'}$ (Table 6 and Fig. 6), a feature which is not found for $\mathbf{1'}$ and $\mathbf{2'}$. The case of $\mathbf{4'}$ is somewhat different, because of the closeness in energy of the occupied Co(II) and Fe(II) 3d levels (Fig. 5). A consequence of this fact is a stronger interaction between the three metal centres and a first ionization potential which is significantly lower than that of the $\mathbf{1'}$–$\mathbf{3'}$ series, in full agreement with the measured redox potential of **4**. Although it was not possible to calculate the dicationic form, we suggest that, similarly as for the $\mathbf{1'}$–$\mathbf{3'}$ series, the first two one-electron oxidations primarily affect the weakly coupled iron centres and the third one corresponds to the oxidation of the Co(II) centre. Finally, we would like to point out on the good agreement between the computed first ionization potentials of the $\mathbf{1'}$–$\mathbf{4'}$ series and the measured first oxidation potentials of the **1**–**4** series, as illustrated by their linear correlation shown in Fig. 7. Such a result brings confidence in the above analysis

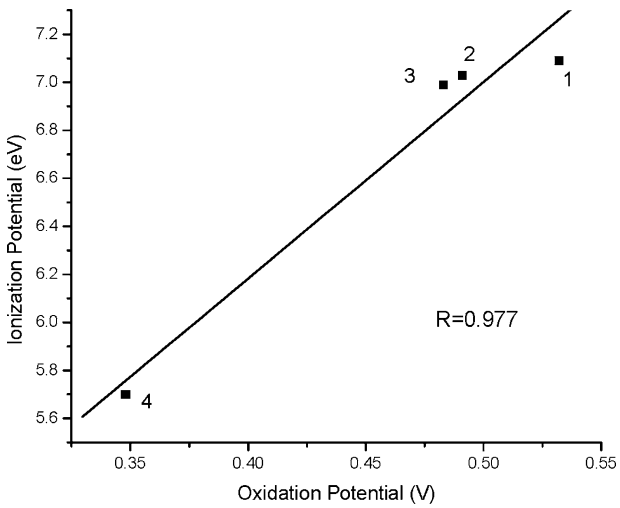

Fig. 7 Plot of the computed first ionization potentials of the $\mathbf{1'}$–$\mathbf{4'}$ series *vs.* the first oxidation potentials of complexes **1**–**4** obtained by cyclic voltammetry (Ag/AgCl, 0.1 M n-$Bu_4N^+PF_6^-$ in CH_2Cl_2).

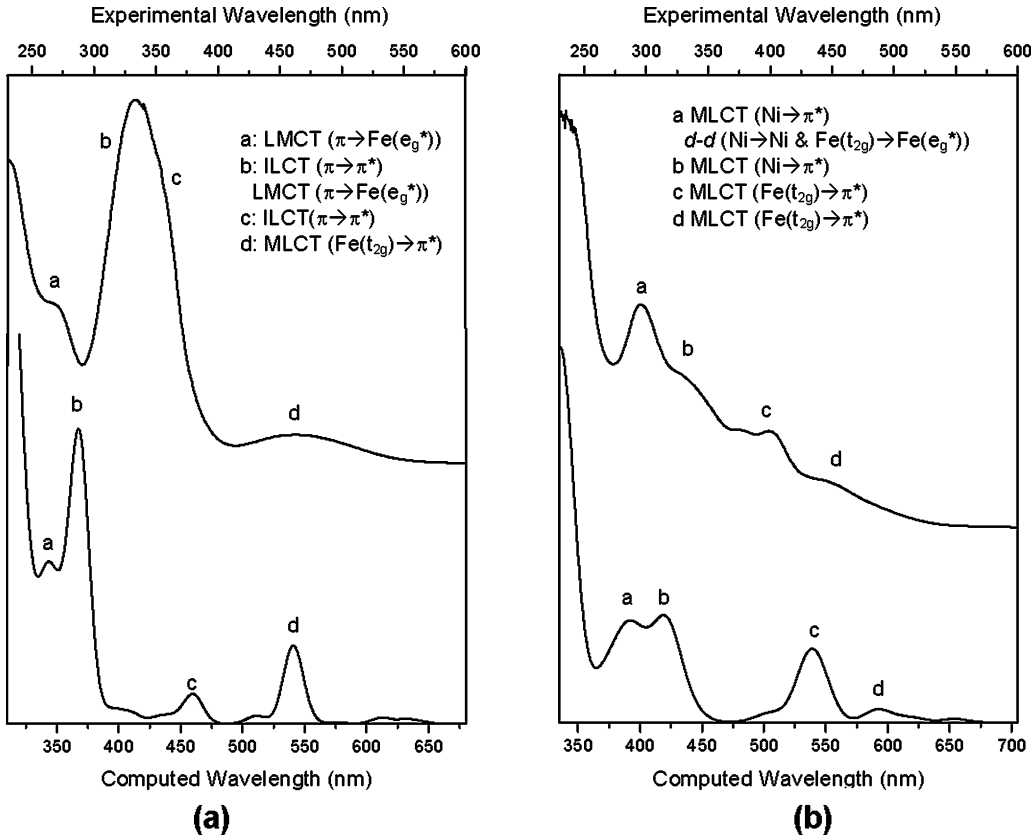

Fig. 8 (a) Experimental (top) and simulated (bottom) UV-Visible spectra of **1** and **1′**, respectively. (b) Experimental (top) and simulated (bottom) UV-Visible spectra of **3** and **3′**, respectively. In all the cases L = bridging ligand.

and conclusions. This prompted us to complement our theoretical investigation in analysing the UV-Visible absorption spectra of these compounds by carrying out TDDFT calculations on the two closed-shell models, namely **1′** and **3′**.

Fig. 8a shows the experimental (top) and theoretical (bottom) UV-Visible spectra of **1** and **1′**, respectively. The theoretical spectrum has been simulated from the computed TDDFT transition wavelengths and oscillator strengths. The major features of the experimental spectrum are acceptably well reproduced by the simulated spectrum, despite of some distortions within the wavelength axis, as is often the case with this type of calculations.[12] This allowed us to propose the a–d band indexation shown in Fig. 8a. The analysis of the major components of the various transitions associated with the computed a–d bands led to the identification of the corresponding charge transfers given in Fig. 8a. Surprisingly, no significant participation of iron d→d charge transfer was found in the investigated energy range. Thus, these transitions are shifted to higher energies due to the presence of a conjugated bridge linking the two ferrocenyl units. Fig. 8b shows the experimental (top) and theoretical (bottom) UV-Visible spectra of **3** and **3′**, respectively. As for the Zn species, the experimental spectrum of **3** is acceptably reproduced, and the low-energy transitions are associated with metal (Fe) to bridging ligand charge transfers in both cases. However, in the case of the Ni species, the transitions lying at higher energy have a major metal (Ni) to bridging ligand character, as well as some iron d→d character.

Concluding remarks

A good understanding of the bonding and electronic properties of the title compounds has emerged from the combination of electrochemical and theoretical results. Communication between the two iron centres is very weak in the case of **1**; it increases when going from **1** to **4** due to the closest proximity in energy of the 3d levels of the central metal to those of iron. Clearly, the central metal plays the role of a third redox centre, at least in the case of **3** and **4**. We are currently investigating the possibility of stabilizing a related species with different central metals. Another way of tuning the electronic communication in these species is to deal with three different metals. This is also under investigation.

Experimental

General remarks

All operations were performed under an inert atmosphere using standard vacuum/dinitrogen line (Schlenk) techniques. Solvents were dried and distilled under dinitrogen by standard methods prior to use. Cobalt(II) acetate tetrahydrate, nickel(II) acetate tetrahydrate, copper(II) acetate monohydrate, zinc(II) acetate dihydrate and ethylenediamine were purchased from commercial suppliers. 1-Ferrocenyl-1,3-butanedione, (η^5-Cp)Fe(η^5-C_5H_4)C(O)CH_2C(O)CH_3 was synthesized according to our recently published procedures.[8] IR spectra were obtained as KBr

disks on a Perkin Elmer model 1600 FT-IR spectrophotometer, in the range of 4000–450 cm^{-1}. Electronic spectra were recorded in CH_2Cl_2 solutions with a Spectronic, Genesys 2 spectrophotometer. ^{1}H-NMR spectra were acquired at 297 K on a multinuclear Bruker AC 400 spectrometer in acetone-d_6. All ^{1}H-NMR chemical shifts were referenced using the chemical shifts of residual solvent resonances. Electrochemical measurements were performed using a Radiometer Analytical model PGZ 100 all-in one potentiostat, using a standard three-electrode setup with a platinum electrode, platinum wire auxiliary electrode and Ag/AgCl as the reference electrode; CH_2Cl_2 solutions of the compound under study were 1.0 mM and 0.1 M in the supporting electrolyte n-$Bu_4N^+PF_6^-$ with the voltage scan rate = 100 mV s^{-1}. Under these experimental conditions the ferrocene/ferricinium couple, used as an internal reference for the potential measurements, was located at $E_{1/2}$ = 0.421 V (ΔE_p = 81 mV). $E_{1/2}$ is defined as equal to $(E_{pa} + E_{pc})/2$, where E_{pa} and E_{pc} are the anodic and cathodic peak potentials, respectively.

Syntheses

General procedure

A round bottom flask with a reflux condenser was charged with 1-ferrocenyl-1,3-butanedione (Hfcbd), 1,2-ethylenediamine and the appropriate metal(II) acetate in a 2 : 2 : 1 molar ratio, before methanol (20 cm^3) was added. The solution was refluxed for 15 h. Cooling the reaction mixture to room temperature led to the precipitation of a solid which was filtered off, washed with diethylether and recrystallized from a CH_2Cl_2–hexane (1 : 1) mixture. Complexes **1–4** were identified by comparison of their melting points, IR and ^{1}H NMR (for diamagnetic Zn(II) and Ni(II) derivatives) data with those reported in the literature.[5]

Ethylenediimine-bis(1-ferrocenyl-1,3-butanedionate)zinc(II) 1. FcBD: 135 mg (0.50 mmol), 1,2-ethylenediamine: 34 mm^3 (0.50 mmol) and $Zn(O_2CCH_3)_2{\cdot}2H_2O$: 55 mg (0.25 mmol); yield: 91 mg, 58%.

Ethylenediimine-bis(1-ferrocenyl-1,3-butanedionate)copper(II) 2

FcBD: 270 mg (1.0 mmol), 1,2-ethylenediamine: 67 mm^3 (1.0 mmol) and $Cu(O_2CCH_3)_2{\cdot}H_2O$: 100 mg (0.5 mmol); yield: 138 mg, 44%.

Ethylenediimine-bis(1-ferrocenyl-1,3-butanedionate)nickel(II) 3. FcBD: 104 mg (0.38 mmol), 1,2-ethylenediamine: 25 mm^3 (0.38 mmol) and $Ni(O_2CCH_3)_2{\cdot}4H_2O$: 48 mg (0.19 mmol); yield: 56 mg, 46%.

Ethylenediimine-bis(1-ferrocenyl-1,3-butanedionate)cobalt(II) 4. FcBD: 108 mg (0.40 mmol), 1,2-ethylenediamine: 27 mm^3 (0.40 mmol) and $Co(O_2CCH_3)_2{\cdot}4H_2O$: 50 mg (0.20 mmol); yield: 55 mg, 44%.

X-Ray crystallographic data for 3†

Orange single crystals of **3** suitable for X-ray diffraction studies were grown from a CH_2Cl_2–hexane mixture. One of these crystals was glued on a glass fiber in a random orientation and mounted on a Bruker Smart Apex diffractometer equipped with a CCD area detector. The highly redundant data collection was performed at room temperature using graphite monochromated Mo-Kα radiation (λ = 0.71073 Å) with separations of 0.3° between frames and 10 s for frame. Data integration was made using SAINT[13] and a multi-scan absorption correction was applied using SADABS.[14] The structure was solved using XS in SHELXTL-PC[15] by direct methods and completed (non-H atoms) by difference Fourier techniques. Refinement until convergence was obtained by full-matrix least-squares on F^2 using SHELXL97.[16] Hydrogen atoms of the methyl groups were positioned at their expected values and allowed to ride in coordinates (C–H = 0.96 Å) as well as in displacements factors (1.5 times their hosts).

Crystallographic data for 3

$C_{30}H_{30}Fe_2N_2NiO_2$, M_r = 620.97 g mol^{-1}, monoclinic, $C2/c$, unit cell dimensions: a = 36.668(3), b = 7.5346(7), c = 23.5074(19) Å, β = 125.8820(10)°, V = 5262.1(8) $Å^3$, Z = 8, D_{calcd} = 1.568 g cm^{-3}, μ = 1.827 mm^{-1}, $F(000)$ = 2560. Data/restraints/parameters: 5906/0/336, R_1/wR_2 ($I > 2\sigma(I)$) = 0.0989/0.1699, R_1/wR_2 (all data) = 0.2261/0.2322, GOF = 0.997, $[\Delta\rho]_{min}/[\Delta\rho]_{max}$: −0.768/0.505.

CCDC reference number 655308.

For crystallographic data in CIF or other electronic format see DOI: 10.1039/b711467b

Computational details

DFT[17] calculations were carried out using the Amsterdam Density Functional (ADF) program.[18] The Vosko–Wilk–Nusair parametrization[19] was used to treat electron correlation within the local density approximation, with gradient corrections added for exchange (Becke88)[20] and correlation (Perdew),[21] respectively. The numerical integration procedure applied for the calculation was developed by te Velde.[17d] The standard ADF TZP basis set was used for all the atoms. The frozen core approximation was used to treat core electrons, at the following level: Zn, 3p; Cu, 3p; Ni, 3p; Co, 3p; Fe, 3p; C, 1s; N, 1s and O, 1s.[17d] Full geometry optimizations were carried out on each complex using the analytical gradient method implemented by Verluis and Ziegler.[22] The geometry for all the model compounds discussed in the text were fully optimized, with a good agreement between the computed geometric parameters and the available structural data. Spin-unrestricted calculations were carried out on all the odd-electrons and open-shell systems. The UV-Visible electronic absorption transitions were computed on the DFT-optimized geometries using the time-dependant density functional theory (TDDFT)[23] method implemented within the ADF program, using the LB94 functional.

Acknowledgements

The authors acknowledge Dr F. Barrière (Rennes) for helpful discussions. Financial support from the Fondo Nacional de Desarrollo Científico y Tecnológico [FONDECYT (Chile); grant no. 3060043 (M. F.) and grant no. 1040851 (C. M. and D. C.)], the ECOS-SUD (France)–CONICYT (Chile) agreement C05E03 (C. M., D. C., M. T. G., J.-R. H. and J.-Y. S.), and the Pontificia Universidad Católica de Valparaíso, Chile (C. M. and D. C.), is gratefully acknowledged.

References

1 (*a*) S. Barlow and D. O'Hare, *Chem. Rev.*, 1997, **97**, 637 and references therein; (*b*) A.-C. Ribou, J.-P. Launay, M. L. Sachtleben, H. Li and C. W. Spangler, *Inorg. Chem.*, 1996, **35**, 3735; (*c*) U. Siemeling and K. Bausch, *Inorg. Chim. Acta*, 2005, **358**, 2146; (*d*) K. R. Justin Thomas, J. T. Lin and Y. S. Wen, *Organometallics*, 2000, **19**, 1008.

2 (*a*) P. Zanello, in *Ferrocenes: Homogenous Catalysis, Organic Synthesis, Materials Science*, ed. A. Togni and T. Hayashi, Wiley-VCH, Weinheim, Germany, 1995, ch. 7, p. 317; (*b*) O. Seidelmann, L. Beyer, R. Richter and T. Herr, *Inorg. Chim. Acta*, 1998, **271**, 40; (*c*) J. H. K. Yip, J. Wu, K.-Y. Wong, K.-W. Yeung and J. J. Vittal, *Organometallics*, 2002, **21**, 1612; (*d*) J. H. K. Yip, J. Wu, K. Y. Wong, K. P. Ho, C. S.-N. Pun and J. J. Vittal, *J. Chin. Chem. Soc.*, 2004, **51**, 1245; (*e*) P. J. Schebler, C. G. Riordan, L. Liable-Sands and A. L. Rheingold, *Inorg. Chim. Acta*, 1998, **270**, 543; (*f*) C.-Y. Duan, Y.-P. Tian, Z.-H. Liu, X.-Z. You and T. C. W. Mak, *J. Organomet. Chem.*, 1998, **570**, 155; (*g*) P. Li, I. J. Scowen, J. E. Davies and M. A. Halcrow, *J. Chem. Soc., Dalton Trans.*, 1998, 3791; (*h*) H.-J. Lee and D.-Y. Noh, *J. Mater. Chem.*, 2000, **10**, 2167; (*i*) P. D. W. Boyd, A. K. Burrell, W. M. Campbell, P. A. Cocks, K. C. Gordon, G. B. Jameson, D. L. Officer and Z. Zhao, *Chem. Commun.*, 1999, 637.

3 P. Zanello, F. Fabrizi de Biani, C. Glidewell, J. Koenig and S. J. Marsh, *Polyhedron*, 1998, **17**, 1795.

4 U. T. Mueller-Westerhoff and R. W. Sanders, *Organometallics*, 2003, **22**, 4778.

5 (*a*) Z. Ying, S. Hong-Sui, H. Guo-Sheng and M. Yong-Xiang, *Transition Met. Chem.*, 1993, **18**, 635; (*b*) Y.-C. Shi, H.-M. Yang, W.-B. Shen, C.-G. Yan and X.-Y. Hu, *Polyhedron*, 2004, **23**, 749.

6 C. Creutz, *Prog. Inorg. Chem.*, 1983, **30**, 1.

7 D. M. D'Alessandro and F. R. Keene, *Dalton Trans.*, 2004, 3950.

8 M. Fuentealba, J.-R. Hamon, D. Carrillo and C. Manzur, *New J. Chem.*, 2007, **31**, 1815.

9 (*a*) A. G. Orpen, L. Brammer, F. H. Allen, D. Kennard, D. G. Watson and R. Taylor, *J. Chem. Soc., Dalton Trans.*, 1989, S1; (*b*) CSD System: F. H. Allen, *Acta Crystallogr., Sect. B*, 2002, **ă58**, 380.

10 N. Faux, F. Robin-Le Guen, P. Le Poul, B. Caro, N. Le Poul, Y. Le Mest, S. J. Green, S. Le Roux, S. Kahlal and J.-Y. Saillard, *Tetrahedron*, 2007, **63**, 7142.

11 (*a*) F. Barrière, N. Camire, W. E. Geiger, U. T. Mueller-Westerhoff and R. Sanders, *J. Am. Chem. Soc.*, 2002, **124**, 7262; (*b*) F. Barrière and W. E. Geiger, *J. Am. Chem. Soc.*, 2006, **128**, 3980.

12 C. Manzur, L. Millán, M. Fuentealba, J.-R. Hamon, L. Toupet, S. Kahlal, J.-Y. Saillard and D. Carrillo, *Inorg. Chem.*, 2007, **46**, 1123.

13 *SAINT (Version 6.02a)*, Bruker Analytical X-ray Systems Inc., Madison, WI, USA, 2000.

14 G. M. Sheldrick, *SADABS: Multi-Scan Absorption Correction Program*, University of Göttingen, Germany, 2001.

15 G. M. Sheldrick, *SHELXTL-PC (version 5.0)*, Siemens Analytical X-ray Instruments Inc., Madison, WI, USA, 1994.

16 G. M. Sheldrick, *SHELXS-97 and SHELXL-97: Programs for Structure Resolution and Structure Refinement*, University of Göttingen, Germany, 1997.

17 (*a*) E. J. Baerends, D. E. Ellis and P. Ros, *Chem. Phys.*, 1973, **2**, 41; (*b*) E. J. Baerends and P. Ross, *Int. J. Quantum Chem.*, 1978, **S12**, 169; (*c*) P. M. Boerrigter, G. te Velde and E. J. Baerends, *Int. J. Quantum Chem.*, 1988, **33**, 87; (*d*) G. te Velde and E. J. Baerends, *J. Comput. Phys.*, 1992, **99**, 84.

18 *Amsterdam Density Functional (ADF) Program*, Vrije Universiteit, Amsterdam, The Netherlands, 2005.

19 S. D. Vosko, L. Wilk and M. Nusair, *Can. J. Chem.*, 1990, **58**, 1200.

20 (*a*) A. D. Becke, *J. Chem. Phys.*, 1986, **84**, 4524; (*b*) A. D. Becke, *Phys. Rev. A*, 1988, **38**, 2098.

21 (*a*) J. P. Perdew, *Phys. Rev. B*, 1986, **33**, 8882; (*b*) J. P. Perdew, *Phys. Rev. A*, 1986, **34**, 7406.

22 L. Verluis and T. Ziegler, *J. Chem. Phys.*, 1988, **88**, 322.

23 (*a*) M. Casida, *Time Dependent Functional Response Theory for Molecules in Recent Advances in Density Functional Methods*, ed. D. P. Chong, World Scientific, Singapore, 1995, vol. 1, p. 155; (*b*) E. U. K. Gross, J. F. Dobson and M. Petersilka, in *Density Functional Theory*, ed. R. F. Nalewajski, Top. Curr. Chem., Springer Series, Heidelberg, Germany, 1996; (*c*) S. J. A. van Gisbergen, J. G. Snijders and E. J. Baerends, *Comput. Phys.*, 1999, **118**, 119.

